CrossMark

J. Fluid Mech. (2016), *vol.* 804, *pp.* 201–223. © Cambridge University Press 2016
doi:10.1017/jfm.2016.510

Internal solitary waves in a two-fluid system with a free surface

Tsubasa Kodaira[1], Takuji Waseda[2], Motoyasu Miyata[3,‡] and Wooyoung Choi[4,†]

[1]Department of Oceanography, Dalhousie University, 1355 Oxford Street, Halifax, NS, Canada

[2]Graduate School of Frontier Sciences, The University of Tokyo, Kashiwa, Chiba 277-8563, Japan

[3]Faculty of Liberal Arts, The Open University of Japan, Chiba 261-8586, Japan

[4]Department of Mathematical Sciences, New Jersey Institute of Technology, Newark, NJ 07102-1982, USA

(Received 13 January 2016; revised 20 July 2016; accepted 27 July 2016; first published online 8 September 2016)

Internal solitary waves in a system of two fluids, silicone oil and water, bounded above by a free surface are studied both experimentally and theoretically. By adjusting an extra volume of silicone oil released from a reservoir, a wide range of amplitude waves are generated in a wave tank. Wave profiles as well as wave speeds are measured using multiple wave probes and are then compared with both the weakly nonlinear Korteweg–de Vries (KdV) models and the strongly nonlinear Miyata–Choi–Camassa (MCC) models. As the density difference between the two fluids in the experiment is relatively small (approximately 14 %), but non-negligible, special attention is paid to the effect of the boundary condition at the top surface. The nonlinear models valid for rigid-lid (RL) and free-surface (FS) boundary conditions are considered separately. It is found that the solitary wave of the FS model for a given amplitude is consistently narrower than that of the RL model and it propagates at a slightly lower speed. Due to strong nonlinearity in the internal-wave motion, the weakly nonlinear KdV models fail to describe the measured internal solitary wave profiles of intermediate and large wave amplitudes. The strongly nonlinear MCC-FS model agrees better with the measurements than the MCC-RL model, which indicates that the free-surface boundary condition at the top surface is crucial in describing the internal solitary waves in the experiment correctly. Leaving the top surface free in the experiment allows us to observe small and relatively short wave packets on the top surface, particularly when the amplitude of the internal solitary wave is large. Once excited, the wave packet is located above the front half of the internal solitary wave and propagates with a speed close to that of the internal solitary wave underneath. A simple resonance mechanism between short surface waves and long internal waves without and with nonlinear effects is examined to estimate the characteristic wavelength of modulated short surface waves, which is found to be in good agreement with the observed wavelength when nonlinearity is taken into account. Using ray theory, the evolution of short surface waves in the presence of

†Email address for correspondence: wychoi@njit.edu
‡Deceased 5 August 2013.

https://doi.org/10.1017/jfm.2016.510 Published online by Cambridge University Press

a background current induced by an internal solitary wave is also investigated to examine the location of the modulated surface wave packet.

Key words: internal waves, solitary waves, stratified flows

1. Introduction

Oceanic internal solitary waves of large amplitude are often generated by the action of tidal currents over bottom topography and have been observed frequently in many coastal regions. The simplest model to describe the propagation of internal solitary waves is the weakly nonlinear Korteweg–de Vries (KdV) equation (Benjamin 1966), where the effects of nonlinear wave steepening and linear wave dispersion are assumed to be balanced. Although the KdV model is widely used due to its simple form, its validity is rather limited to small-amplitude waves. For example, the KdV solitary wave is too narrow and moves too fast in comparison with laboratory or field observations (see Grue *et al.* 1999). Higher-order weakly nonlinear models have also been proposed by including higher-order nonlinear and/or dispersive terms (see, for example, Koop & Butler 1981). These models provide improved comparisons with observations, but, due to the weakly nonlinear assumption in their derivation, fail to capture a number of characteristics of large-amplitude internal solitary waves.

To take into account strong nonlinearity of large-amplitude internal solitary waves, for a two-layer system bounded above by a rigid surface, Miyata (1988) and Choi & Camassa (1999) derived a theoretical model by assuming that the characteristic wavelength is long compared with the total fluid depth, but the wave amplitude is comparable to the total fluid depth. This strongly nonlinear long-wave model is often referred to as the MCC model in the literature and is an unsteady generalization of the steady long-wave model of Miyata (1985). In comparison with laboratory experiments, it has been shown that the MCC model derived under the rigid-lid approximation successfully describes the propagation of large-amplitude internal solitary waves in two-layer settings (Choi & Camassa 1999; Camassa *et al.* 2006).

In the majority of previous theoretical studies of internal solitary waves, it is common to assume that the top surface is rigid under the so-called rigid-lid approximation. When the density difference between two neighbouring layers is relatively small, for example as in oceanic conditions, it can be shown that the ratio between the displacement of the top free surface and that of the interface is proportional to the density jump (see § 2). In laboratory experiments where fresh water and brine were used for stratification (Segur & Hammack 1982; Kao, Pan & Renouard 1985; Grue *et al.* 1999), the density difference and, therefore, the displacement of the top free surface were small, so that it was reasonable to compare the laboratory experiments with a model under the rigid-lid approximation. On the other hand, in some laboratory experiments (Walker 1973; Koop & Butler 1981; Michallet & Barthelemy 1998), the density differences were non-negligible, but most comparisons of their measurements were made with theoretical models under the rigid-lid approximation and little attention was paid to the free surface. Theoretically, Moni & King (1995) studied the steady Euler equations for a two-layer system with a free surface, but computed only surface solitary wave solutions, while Peters & Stoker (1960) considered weakly nonlinear solitary waves using the KdV model. To the best of our knowledge, large-amplitude internal solitary waves propagating under the top free surface in a two-layer system of constant densities have not been investigated

https://doi.org/10.1017/jfm.2016.510 Published online by Cambridge University Press

systematically yet. In addition, it is important to allow the top surface to be free when the interaction of internal solitary waves with relatively short surface waves is investigated to better understand their surface expressions appearing on satellite images (Liu *et al.* 1998).

In this paper, free-surface effects on large-amplitude internal solitary waves are examined experimentally in a system of two immiscible fluids with a non-negligible density jump, and the measurements are compared with the strongly nonlinear model valid for the case when the top boundary is free (Choi & Camassa 1996; Barros, Gavrilyuk & Teshukov 2007), which is the generalization of the MCC model. In particular, we focus on the change in internal solitary wave profiles in the presence of the top free surface and the appearance of short surface wave packets above the internal solitary waves.

This paper is organized as follows. The model equations for internal solitary waves are presented in § 2. After describing the configuration of laboratory experiments in § 3, the measured wave profiles and wave speed of the internal solitary waves are compared with the theoretical solutions in § 4. Short surface wave packets observed during some of the laboratory experiments are described and their generation mechanisms are discussed in § 5. Then, concluding remarks are given in § 6.

2. Model equation

Consider a system of two fluid layers whose densities and thicknesses are given by ρ_i and h_i respectively, with $i=1$ for the upper fluid layer and $i=2$ for the lower layer. When the characteristic wavelength λ is long compared with the total fluid depth so that $\epsilon=(h_1+h_2)/\lambda\ll 1$, the strongly nonlinear models can be derived when the top surface is either rigid (Miyata 1988; Choi & Camassa 1999) or free (Choi & Camassa 1996; Barros *et al.* 2007).

2.1. *The MCC-RL model*

The MCC model under the rigid-lid assumption can be written, in terms of four unknowns (ζ, $\overline{u}_1$, $\overline{u}_2$, P), as

$$\eta_{it}+(\eta_i\overline{u}_i)_x=0, \tag{2.1}$$

$$\overline{u}_{it}+\overline{u}_i\overline{u}_{ix}+g\zeta_x=-\frac{P_x}{\rho_i}+\frac{1}{\eta_i}\left(\frac{1}{3}{\eta_i}^3G_i\right)_x, \tag{2.2}$$

where ζ is the elevation of the interface, P is the pressure at the interface, and $\overline{u}_i$ ($i=1,2$) are the depth-averaged horizontal velocities, defined by

$$\overline{u}_i(x,t)=\frac{1}{\eta_i}\int_{[\eta_i]}u_i(x,z,t)\,\mathrm{d}z, \tag{2.3}$$

with $\int_{[\eta_i]}$ denoting $\int_{\zeta}^{h_1}$ or $\int_{-h_2}^{\zeta}$ for $i=1$ or 2 respectively. Here, g is the gravitational acceleration, η_i are the local layer thicknesses defined by

$$\eta_1=h_1-\zeta, \quad \eta_2=h_2+\zeta \tag{2.4a,b}$$

and G_i are given by

$$G_i(x,t)=\overline{u}_{ixt}+\overline{u}_i\overline{u}_{ixx}-(\overline{u}_{ix})^2=-\frac{(D_i{}^2\eta_i)}{\eta_i}, \tag{2.5}$$

https://doi.org/10.1017/jfm.2016.510 Published online by Cambridge University Press

where $D_i \equiv \partial_t + \overline{u}_i \partial_x$ and we have used (2.1) for the last equality. The kinematic equations given by (2.1) are exact while the dynamic equations given by (2.2) have an error of $O(\epsilon^4)$. To distinguish it from the free-surface model introduced in the following section, the system for a top rigid lid given by (2.1)–(2.2) will be referred to as MCC-RL.

When a solitary wave is assumed to propagate, without change of form, with constant speed c, one can write η_i and u_i, in the frame of reference moving with the solitary wave, as

$$\eta_i = \eta_i(X), \quad \overline{u}_i = \overline{u}_i(X), \quad X = x - ct. \tag{2.6a–c}$$

After substituting (2.6) into (2.1), integrating the resulting equation once with respect to X, and imposing the boundary conditions at infinities ($\eta_1 \to h_1$, $\eta_2 \to h_2$ and $\overline{u}_i \to 0$ as $X \to \pm\infty$), $\overline{u}_i$ can be expressed in terms of η_i as

$$\overline{u}_i = c\left(1 - \frac{h_i}{\eta_i}\right). \tag{2.7}$$

Then, after eliminating P from (2.2) for $i = 1, 2$ and substituting (2.7) for $\overline{u}_i$ into the resulting equation, one can obtain a single nonlinear ordinary differential equation for ζ (Miyata 1985):

$$\zeta_X{}^2 = \frac{3\zeta^2[c^2(\rho_1\eta_2 + \rho_2\eta_1) - g(\rho_2 - \rho_1)\eta_1\eta_2]}{c^2(\rho_1 h_1{}^2\eta_2 + \rho_2 h_2{}^2\eta_1)}. \tag{2.8}$$

From $\zeta_X = 0$ when $\zeta = a$, the relationship between the solitary wave speed c and its amplitude a is given (Choi & Camassa 1999) by

$$\frac{c^2}{c_0{}^2} = \frac{(h_1 - a)(h_2 + a)}{h_1 h_2 - (c_0{}^2/g)a}, \tag{2.9}$$

where linear long-wave speed c_0 is given by

$$c_0{}^2 = \frac{g h_1 h_2(\rho_2 - \rho_1)}{\rho_1 h_2 + \rho_2 h_1}. \tag{2.10}$$

The solitary wave solution satisfying $\zeta \to 0$ as $X \to \infty$ can be found, by integrating (2.8) numerically, up to the maximum wave amplitude a_m and its corresponding speed c_m given by

$$a_m = \frac{h_1 - h_2\sqrt{\rho_1/\rho_2}}{1 + \sqrt{\rho_1/\rho_2}}, \quad c_m{}^2 = g(h_1 + h_2)\frac{1 - \sqrt{\rho_1/\rho_2}}{1 + \sqrt{\rho_1/\rho_2}}. \tag{2.11a,b}$$

2.2. *The MCC-FS model*

When the upper layer is bounded above by the top free surface located at $z = h_1 + \zeta_1$ and below by the interface located at $z = \zeta_2$, the strongly nonlinear model (MCC-FS)

https://doi.org/10.1017/jfm.2016.510 Published online by Cambridge University Press

with error of $O(\epsilon^4)$ is given (Choi & Camassa 1996; Barros *et al.* 2007) by

$$\eta_{1t} + (\eta_1 \bar{u}_1)_x = 0, \quad \eta_1 = h_1 + \zeta_1 - \zeta_2, \tag{2.12a,b}$$

$$\eta_{2t} + (\eta_2 \bar{u}_2)_x = 0, \quad \eta_2 = h_2 + \zeta_2, \tag{2.13a,b}$$

$$\bar{u}_{1t} + \bar{u}_1 \bar{u}_{1x} + g(\eta_1 + \eta_2)_x = \frac{1}{\eta_1}\left(\frac{1}{3}{\eta_1}^3 G_1\right)_x - \frac{1}{\eta_1}\left(\frac{1}{2}{\eta_1}^2 {D_1}^2 \eta_2\right)_x + \left(\frac{1}{2}\eta_1 G_1 - {D_1}^2 \eta_2\right)\eta_{2x}, \tag{2.14}$$

$$\bar{u}_{2t} + \bar{u}_2 \bar{u}_{2x} + g\left(\frac{\rho_1}{\rho_2}\eta_1 + \eta_2\right)_x = \frac{1}{\eta_2}\left(\frac{1}{3}{\eta_2}^3 G_2\right)_x + \frac{\rho_1}{\rho_2}\left(\frac{1}{2}{\eta_1}^2 G_1 - \eta_1 {D_1}^2 \eta_2\right)_x, \tag{2.15}$$

where $\bar{u}_i$ are the depth-averaged velocities defined by (2.3) with $\int_{[\eta_i]}$ defined as $\int_{\zeta_2}^{h_1+\zeta_1}$ or $\int_{-h_2}^{\zeta_2}$ for $i = 1$ or 2 respectively.

When the system given by (2.12)–(2.15) is linearized and its dispersive terms on the right-hand sides are neglected, one can obtain the linear long-wave speed c_0 by solving

$${c_0}^4 - g(h_1 + h_2){c_0}^2 + g^2 h_1 h_2 \left(1 - \frac{\rho_1}{\rho_2}\right) = 0, \tag{2.16}$$

which yields the linear long-wave speeds of the faster barotropic ($c_0{}^+$) and slower baroclinic ($c_0{}^-$) modes. The ratio between the free-surface and interface displacements is given by

$$\frac{\zeta_1}{\zeta_2} = \frac{{c_0}^2}{{c_0}^2 - g h_1}. \tag{2.17}$$

As it can be shown that $(c_0{}^-)^2 < g h_1 < (c_0{}^+)^2$, the free surface and the interface are in phase ($\zeta_1/\zeta_2 > 0$) for the barotropic mode while they are out of phase ($\zeta_1/\zeta_2 < 0$) for the baroclinic mode.

For most previous experiments with $\Delta = (\rho_2 - \rho_1)/\rho_2 \ll 1$, the long-wave speeds can be approximated by

$$(c_0^+)^2 = g(h_1 + h_2)\left[1 - \frac{h_1 h_2}{(h_1 + h_2)^2}\Delta + O(\Delta^2)\right], \quad (c_0^-)^2 = \frac{g h_1 h_2}{(h_1 + h_2)}\Delta + O(\Delta^2), \tag{2.18a,b}$$

where $\pm$ represent the barotropic and baroclinic internal-wave modes respectively. Then, the amplitude ratios for the two wave modes can be approximated, from (2.17), by

$$\left(\frac{\zeta_1}{\zeta_2}\right)^+ = \left(\frac{h_1 + h_2}{h_2}\right)[1 + O(\Delta)], \quad \left(\frac{\zeta_1}{\zeta_2}\right)^- = -\left(\frac{h_2}{h_1 + h_2}\right)\Delta[1 + O(\Delta)]. \tag{2.19a,b}$$

From (2.19), since $(\zeta_1/\zeta_2)^- = O(\Delta)$, the displacement of the top free surface can be neglected for the baroclinic mode for $\Delta \ll 1$, which most oceanic conditions satisfy. On the other hand, in our experiments, Δ is not negligibly small (approximately 0.14), and the effect of the top free surface could be necessary in the description

https://doi.org/10.1017/jfm.2016.510 Published online by Cambridge University Press

of the internal-wave motions. It should be noticed that this discussion about the free-surface effect should be applied to internal solitary waves in a two-layer system of constant densities. For example, it provides no explanation of the role of a top free surface on the instability of internal solitary waves observed previously in laboratory experiments (Grue *et al.* 2000; Carr *et al.* 2008; Luzzatto-Fegiz & Helfrich 2014) with linearly stratified fluids, in which recirculating cores could appear as the wave amplitude increases (Goullet & Choi 2008; Fructus *et al.* 2009). No internal solitary waves with such recirculating cores are possible in the two-layer system considered here.

For travelling solitary waves, in the frame of reference moving with wave speed c as in (2.6), the system can be reduced to the following nonlinear system of coupled second-order differential equations (see appendix A for its derivation):

$$\alpha_{j1}\eta_1'' + \alpha_{j2}\eta_2'' + \alpha_{j3}\eta_1'^2 + \alpha_{j4}\eta_2'^2 + \alpha_{j5}\eta_1'\eta_2' = \alpha_{j6} \quad \text{for } j = 1, 2, \tag{2.20}$$

where the prime denotes differentiation with respect to X and the nonlinear coefficients α_{jk} can be found in appendix A. This steady system is identical to that obtained by Barros & Gavrilyuk (2007) using the Lagrangian formulation. To find its solitary wave solutions, the system should be solved numerically for a given wave speed c. While two different linear wave speeds (c_0^+ for barotropic waves and c_0^- for baroclinic waves) are possible, internal solitary wave profiles are computed by choosing $c \to c_0^-$ in the limit of zero wave amplitude. Unlike the rigid-lid case, no explicit relationship between wave speed and wave amplitude is known and should be computed numerically.

2.3. *The weakly nonlinear uni-directional model*

For uni-directional waves, under the weakly nonlinear assumption, the MCC-RL and MCC-FS can be reduced to the KdV equation for the interface displacement ζ_2 (with $\zeta_2 = \zeta$ for the rigid-lid case):

$$\zeta_{2t} + c_0\zeta_{2x} + c_1\zeta_2\zeta_{2x} + c_2\zeta_{2xxx} = 0, \tag{2.21}$$

where c_i are given for the rigid-lid case by

$$c_1 = \frac{-3c_0}{2}\frac{\rho_1 {h_2}^2 - \rho_2 {h_1}^2}{\rho_1 h_1 {h_2}^2 + \rho_2 {h_1}^2 h_2}, \quad c_2 = \frac{c_0}{6}\frac{\rho_1 {h_1}^2 h_2 + \rho_2 h_1 {h_2}^2}{\rho_1 h_2 + \rho_2 h_1}, \tag{2.22a,b}$$

while they are given for the free-surface case by

$$c_1 = \frac{3c_0}{2h_2}\frac{1 + (\rho_1/\rho_2)h_1{h_2}^2/({c_0}^2/g - h_1)^3}{1 + (\rho_1/\rho_2)h_1 h_2/({c_0}^2/g - h_1)^2}, \tag{2.23a}$$

$$c_2 = \frac{c_0 {h_2}^2}{6}\frac{1 + (\rho_1/\rho_2)(h_1/h_2)[3 + 3h_1/({c_0}^2/g - h_1) + {h_1}^2/({c_0}^2/g - h_1)^2]}{1 + (\rho_1/\rho_2)h_1 h_2/({c_0}^2/g - h_1)^2}. \tag{2.23b}$$

The solitary wave solution of the KdV equation can be written as

$$\zeta_2(X) = a\,\mathrm{sech}^2(X/\lambda_{KdV}), \quad X = x - c_{KdV}t, \tag{2.24a,b}$$

where the characteristic length scale λ_{KdV} and the wave speed c_{KdV} are given, respectively, by

$${\lambda_{KdV}}^2 = 12c_2/(ac_1), \quad c_{KdV} = c_0 + c_1 a/3. \tag{2.25a,b}$$

https://doi.org/10.1017/jfm.2016.510 Published online by Cambridge University Press

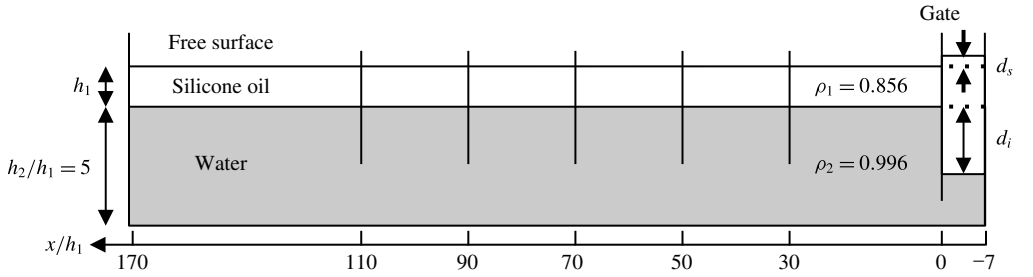


FIGURE 1. Experimental set-up for the internal solitary wave generation in a two-fluid system with a free surface. The top layer is filled with the silicone oil SF1000NFC150 and the bottom layer is filled with water. The top layer thickness is $h_1 = 0.05$ m while the lower layer thickness is $h_2 = 0.25$ m. The specific gravities of silicone oil and water are denoted by ρ_1 and ρ_2 respectively. Five capacitance-type probes represented by black vertical lines are installed at a regular interval of 20 non-dimensional lengths. To generate internal solitary waves of five different wave amplitudes, the interface displacement is adjusted to $d_i/h_1 = 0.6,\ 1.2,\ 1.8,\ 2.4$ and 3.0.

3. Laboratory experiments

3.1. *Two-fluid system*

An immiscible two-fluid system is set up in an approximately 8.5 m long, 0.47 m wide and 0.35 m deep water tank in the Korea Advanced Institute of Science and Technology (KAIST). The bottom layer is a 0.25 m thick water layer and the top layer is a 0.05 m thick silicone oil layer. When necessary, physical variables are non-dimensionalized with respect to the top layer thickness h_1 and the gravitational acceleration g. A vertical gate is installed 0.35 m away from one end of the tank in order to generate internal solitary waves by lifting the gate. The profiles of internal solitary waves are measured using five capacitance-type wave probes. The experimental configuration is schematically shown in figure 1.

The kinematic viscosity of the silicone oil SF1000NFC150 used in the experiment is only 1.5 times greater than that of water based on the material safety data sheet, and we assume that the inviscid assumption can be used in modelling our experiments. The specific densities of the silicone oil and water are measured using a density meter. The specific gravity of the oil is 0.856 ± 0.001 and that of the water is 0.996 ± 0.002 at a temperature of $15 \pm 1\,^{\circ}\mathrm{C}$. Therefore, the dimensionless density difference Δ defined by $\Delta = (\rho_2 - \rho_1)/\rho_2$ is approximately 0.14. The fluctuation of specific density of each fluid is due to either thermal expansion of the fluid or the measurement error mainly caused by the meniscus effect on the wall of the density meter.

With the current experimental set-up with the top free surface, the phase speed of linear long internal waves is given, from (2.16), by $c_0 = 0.242$ m s^{-1}. If the top boundary is rigid, the phase speed increases to 0.255 m s^{-1}. The difference between the two phase speeds is approximately 5 % of c_0, which cannot be neglected for the phase speed measurement.

3.2. *Internal solitary wave generation*

The method to generate internal solitary waves is the same as that of Michallet & Barthelemy (1998). By adjusting the interfacial displacement d_i behind the gate, internal solitary waves of a wide range of amplitudes are generated (figure 1). Since

https://doi.org/10.1017/jfm.2016.510 Published online by Cambridge University Press

the gate is not fully closed to the bottom before the gate is lifted, the water can flow freely below the gate. As a result, the surface behind the gate rises to balance the bottom pressure difference produced by the displaced interface behind the gate. As long as the system is hydrostatically balanced, the surface elevation d_s is estimated to be

$$d_s = \left(\frac{\rho_2 - \rho_1}{\rho_1 + \rho_2}\right) d_i. \tag{3.1}$$

The estimation based on the isostasy (3.1) agrees well with the values measured before the experiments start. Five different interface displacements $d_i/h_1 = (0.6, 1.2, 1.8, 2.4, 3.0)$ are chosen and each experiment is repeated five times to reduce random experimental errors. Then, the wave amplitudes are determined from the measurements at the fifth wave probe by taking an average over the five repetitions. The emerging solitary wave amplitudes $a/h_1 = (0.24, 0.50, 0.77, 0.99, 1.21)$ are used to name each experiment. For example, case 0.24 represents the experiment for the solitary wave whose dimensionless amplitude is 0.24.

The gate is not completely pulled out of the oil layer, but stopped just below the top free surface to minimize the generation of barotropic surface waves. Nevertheless, small-amplitude surface waves are always observed. They propagate faster than the internal waves and are reflected back from the end of the tank. To avoid any possible contamination of internal solitary wave measurements, the reflection of fast-propagating small-amplitude surface waves is suppressed by loose nets, as wave absorbers, placed at the end of the tank.

3.3. *Measurement techniques*

The generated internal solitary waves are measured by capacitance-type wave probes with a sampling frequency of 200 Hz. The capacitance-type wave probe was originally designed to measure the displacement of the air–water interface, and care should be taken for the oil–water interface. A previous experimental study (Walker 1973) with Humble oil (Varsol I) and water neglected any influence of the oil on the wave probe measurement because the wave probe was 550 times less sensitive to the Humble oil than water. On the other hand, our wave probes are on average only 31 times less sensitive to the silicone oil than to the water.

To take into account the influence of the silicone oil on the internal displacement estimation, we use the following formula to determine the interface displacement ζ_2 from the output voltage V of the wave probe:

$$V = C_w\zeta_2 + C_o(\zeta_1 - \zeta_2), \tag{3.2}$$

where C_w and C_o are the calibration coefficients for water and silicone oil respectively, and ζ_1 is the surface displacement. After using (2.17) to estimate the ratio between ζ_1 and ζ_2, the interfacial displacement ζ_2 can be determined from (3.2) for the given output voltage V. The second term on the right-hand side of (3.2) is smaller than the first term as $C_o \ll C_w$, as stated above. The resultant difference of the interface displacement ζ_2 is 3.65 % on average when the effect of the upper oil layer is included.

The accuracy of the measured displacements based on (2.17) and (3.2) is verified with another independent measurement using a digital camera that is placed in front of the third wave probe located at $x/h_1 = 70$. The wave amplitude is read from the images captured by the camera within a possible error of 0.5 mm, or 1 % of the top layer thickness. A ruler is also positioned inside the tank to take into account optical refraction by the glass wall. As a result, little discrepancy is found between the measured amplitudes using the two different methods (figure 2).

https://doi.org/10.1017/jfm.2016.510 Published online by Cambridge University Press

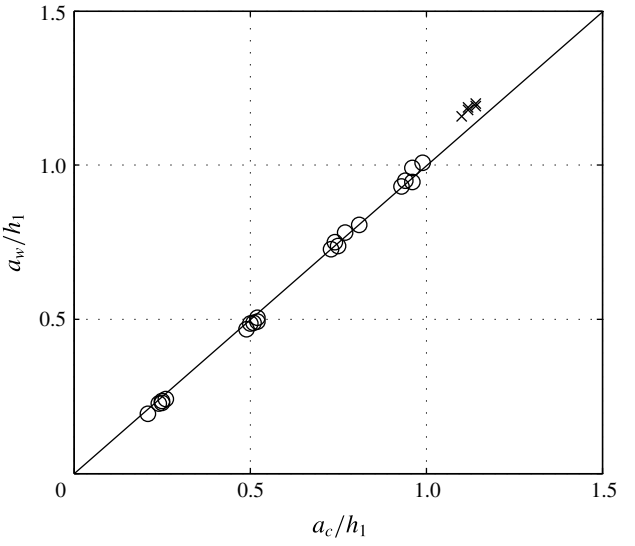


FIGURE 2. Comparison between the wave amplitudes measured at $x/h_1 = 70$ by a digital camera, a_c, and by a wave probe, a_w. The $\times$ marks are for case 1.21 in which the internal solitary waves are perturbed greatly by the Kelvin–Helmholtz instability.

3.4. *Measurement errors*

Both random noise and bias may contaminate experimental data. The device-originated mechanical noise is reduced by taking a running average over 20 sample points, whose time duration is 0.1 s. Other random noise may be produced by imperfectly set interface levels behind the gate and manual lifting of the gate. The random noise is reduced by taking the average over five repeated measurements for each configuration. However, bias is not removed by this averaging process.

Possible factors to produce bias are the thermal expansion of the two fluids during the experiments and the installed position of the sensing wires. The thermal expansion mainly influences the internal solitary wave speed. The linear phase speed of internal waves increases by, at most, 0.99 % when the specific gravity of the oil changes from 0.856 to 0.855 and the specific gravity of the water changes from 0.996 to 0.998. The position of a sensing wire also has an error of 0.01 m due to technical difficulties in its installation. The expected error in the phase speed from the installation position is estimated to be approximately 1 %. Since the error is smaller than the differences between the various theoretical models used for the comparison, the measurements are considered to be reliable to determine the validity of the theoretical models.

4. Results

4.1. *Wave profiles*

As the gate is lifted, the initially displaced interface disintegrates into a leading solitary wave and a dispersive tail, as shown in figure 3. Comparison between the five repeated measurements shown in each panel of figure 3 indicates that the experiments are repeatable. Then, the measured wave profiles are averaged over five repetitions by specifying the maximum correlation coefficient with one of the five records. Leading solitary waves are clearly detected even by the first wave probe without any significant

https://doi.org/10.1017/jfm.2016.510 Published online by Cambridge University Press

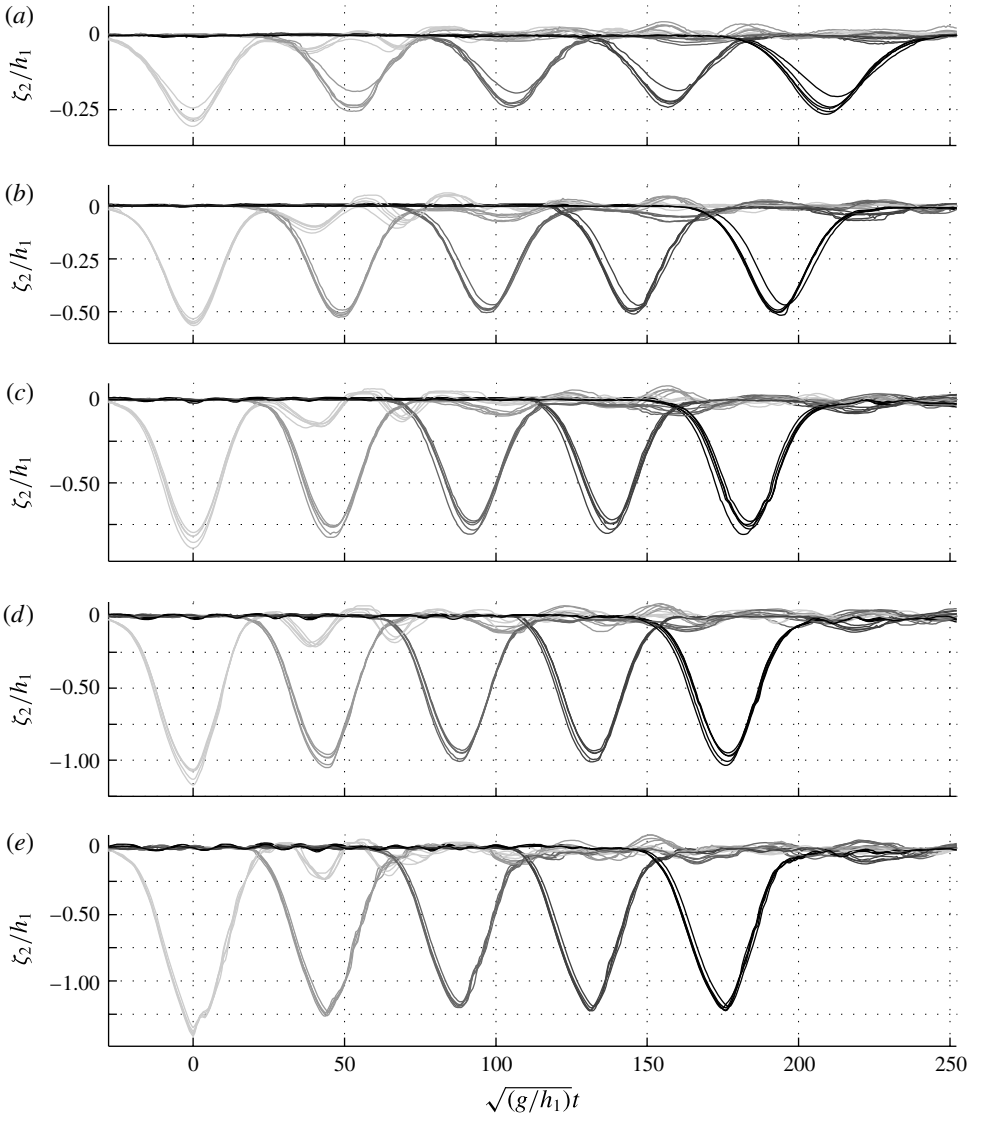


FIGURE 3. Measured interfacial displacements at the five wave probes, non-dimensionalized by the top layer thickness h_1: (*a*) case 0.24, (*b*) case 0.50, (*c*) case 0.77, (*d*) case 0.99 and (*e*) case 1.21. The dimensionless time for each case is set to zero when the first wave probe records the largest displacement. The lines represent experimental data with changing colours from light grey to black for the first to fifth wave probes.

contamination from dispersive tails. The amplitude of the leading solitary wave is then observed to decrease as it propagates downstream, in particular to the second wave probe, beyond which it remains approximately unchanged. The initial decrease of the amplitude implies that the solitary wave needs some time before it reaches a steady state. Theoretical wave profiles are hence compared with the measurement at the fifth wave probe to avoid the initially transient effects. As the wave amplitude increases, the leading solitary wave arrives earlier at wave probes located further

https://doi.org/10.1017/jfm.2016.510 Published online by Cambridge University Press

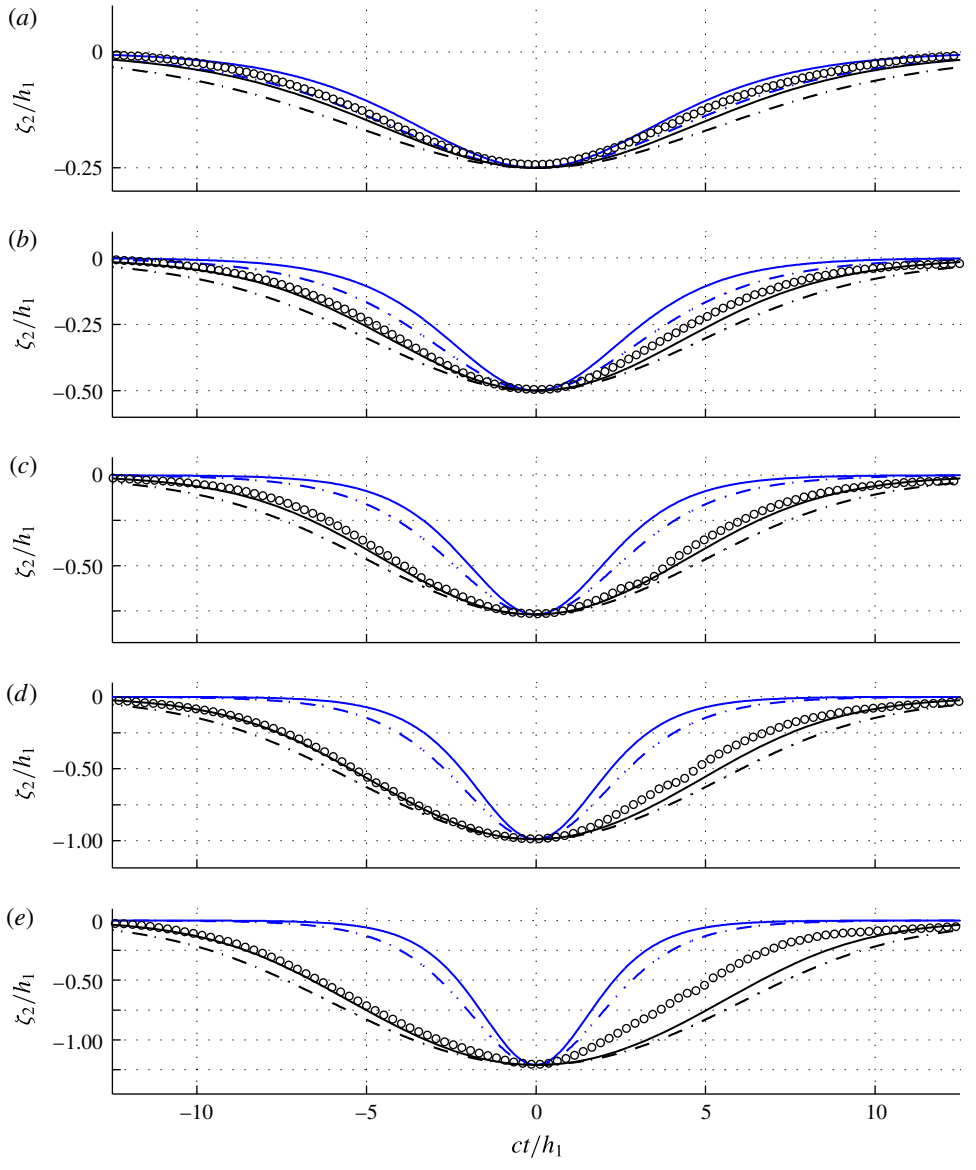


FIGURE 4. (Colour online) Comparison of internal solitary wave profiles between experiments and theoretical models: (*a*) case 0.24, (*b*) case 0.50, (*c*) case 0.77, (*d*) case 0.99 and (*e*) case 1.21. The profiles are non-dimensionalized by using the top layer thickness h_1 and each wave speed c measured by the fourth and fifth wave probes. Circles, experimental data averaged over the five repetitions; black line, MCC-FS; black dashed line, MCC-RL; blue line, KdV-FS; blue dashed line, KdV-RL.

downstream, as expected. The relationship between the wave amplitude and the speed will be discussed in detail in the following section.

For the smallest-amplitude case shown in figure 4(*a*), the averaged wave profile agrees well with the solitary wave solutions of the weakly nonlinear KdV-RL model and the strongly nonlinear MCC-FS model. On the other hand, the KdV-FS equation

https://doi.org/10.1017/jfm.2016.510 Published online by Cambridge University Press

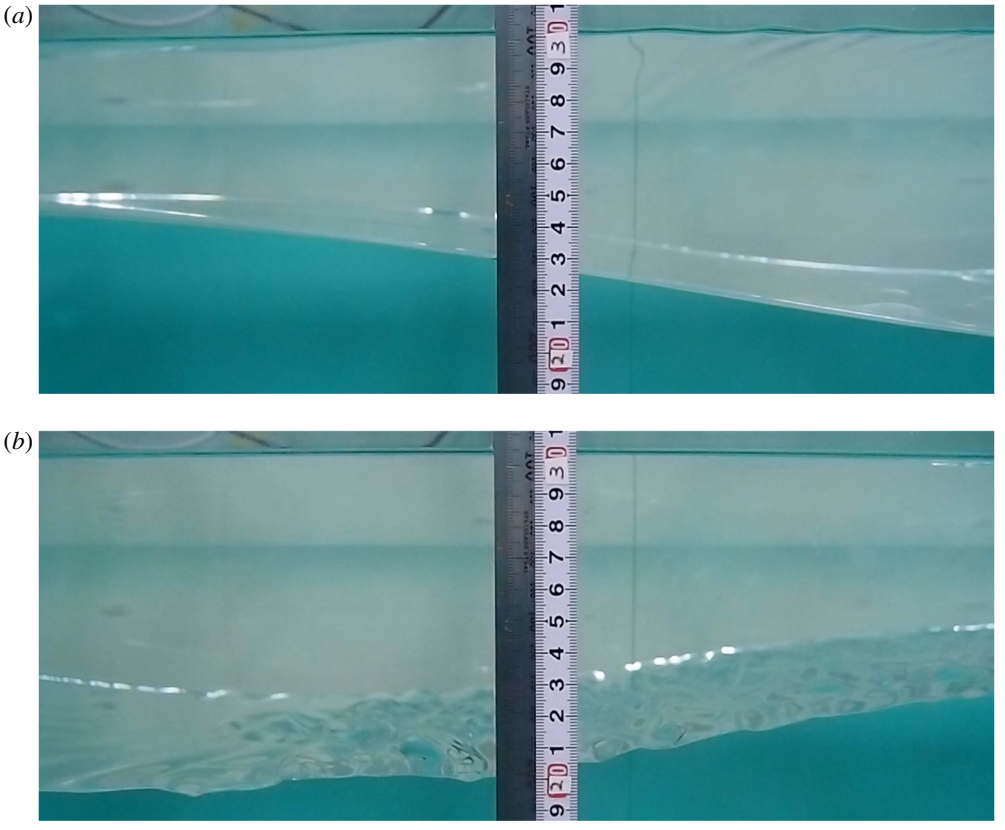


FIGURE 5. (Colour online) An internal solitary wave recorded by a digital camera during the experiment of case 1.21 for (*a*) the front half and (*b*) the rear half (i.e. the solitary wave propagates to the left). The pictures are taken just in front of the third wave probe located at $x/h_1 = 70$. The ruler in cm shown in the figure shows the spatial scale of the internal-wave motion. The appearance of short surface waves on the top free surface can also be observed on the top of snapshot (*a*) and is discussed in § 5.

underestimates the interfacial displacement while the strongly nonlinear MCC-RL model overestimates it. As the amplitude increases (figure 4*b–d*), the measured wave profiles consistently show good agreement only with the MCC-FS model. The solitary wave profiles from both the KdV-RL equation and the KdV-FS equation are narrower than the measured wave profiles, while the wave profiles from the MCC-RL model are broader. Therefore, it can be concluded that an internal solitary wave propagating under a top free surface is always narrower than that under a rigid lid, which has not been confirmed experimentally before. In addition, when the internal solitary wave propagates, it is observed that the top free surface is clearly displaced in the opposite direction to the interfacial displacement (see figure 5). Thus the free-surface boundary condition at the top surface is important to correctly describe the profiles of the internal solitary waves observed in our experiments even though the density difference ($\Delta = 0.14$) is relatively small.

The wave profiles are almost symmetric for small and intermediate wave amplitudes in figure 4(*a–c*), but show some asymmetry, in particular, when the amplitude is almost comparable to the top layer thickness (figure 4*d*,*e*). The asymmetry could be

https://doi.org/10.1017/jfm.2016.510 Published online by Cambridge University Press

caused in part by the slight unsteadiness of the experiment, but it is pronounced in figure 4(*e*), where the internal solitary wave suffers from the Kelvin–Helmholtz (KH) instability excited by the large shear across the interface. Figure 5(*b*) for case 1.21 captures unstable short internal waves that appear on the rear part of the leading internal solitary wave, while the front part shown in figure 5(*a*) is smooth. A similar observation was made in the salt water experiment of Grue *et al.* (1999). It should be pointed out that the surface tension between the two immiscible fluids (oil and water) is non-negligible and plays a stabilizing role when the KH instability is excited. Therefore, in contrast to previous experiments with salt water, no overturning KH billows are observed. This implies that the shear induced across the interface by an internal solitary wave is finite, but is not large enough to overcome the surface tension effect. While three-dimensional disturbances are observed, as shown in figure 5(*b*), the wave probe measurements are taken along the centreline of the tank. We should also remark that, while short-wavelength disturbances on the interface are excited initially when the gate is lifted, they are hardly observed as the internal solitary waves of small or intermediate wave amplitude propagate downstream.

4.2. *Wave speed*

The wave speed of the leading internal solitary wave is determined based on the time interval between its arrival at two adjacent wave probes. The interval is determined to maximize the cross-correlation between the two time series. Since there are five wave probes, the wave speed is estimated at four locations (i.e., $x/h_1 = 40$, 60, 80 and 100). The amplitudes at the four locations are determined as an average of the amplitudes measured by two adjacent wave probes. The relationship between wave speed and wave amplitude is shown in figure 6 for five different cases. As observed previously from the wave profile measurements, figure 6 again shows that the leading solitary wave is significantly attenuated after it is released from the gate, but remains almost unchanged after it passes the third wave probe. The initial decrease of wave amplitude over the first two wave probe locations is greater than the standard deviation of the five repeated measurements, but, after the leading wave passes the third wave probe, the variation of wave amplitude and wave speed is comparable to the standard deviation.

The measured relationship between wave speed and wave amplitude is compared with various theoretical models in figure 6. The weakly nonlinear models obviously overestimate the wave speeds of large-amplitude internal solitary waves. As the experimental data for intermediate wave amplitudes lie between the two strongly nonlinear MCC models, it is difficult to draw a conclusion on the validity of the two strongly nonlinear models in terms of wave speed measurements. For our experimental set-up, the difference in wave speed between the rigid-lid and free-surface cases is theoretically as large as 5 % for small-amplitude waves, but decreases to approximately 1.5 % for large-amplitude waves, which is comparable to the possible measurement error, which was estimated to be at most 2 % in § 3.4. Nevertheless, a significant discrepancy from the rigid-lid model can be clearly observed for smaller-amplitude cases, for example case 0.26. Since its agreement with the wave speed measurements along with our observation of wave profiles is noticeable for a wide range of wave amplitudes, the strongly nonlinear MCC-FS model is relevant for our experiments with the top free surface.

5. Short surface waves above internal solitary waves

When the amplitude of an internal solitary wave is relatively large ($a/h_1 \geqslant 0.77$), short surface waves are often observed on the top free surface, approximately right

https://doi.org/10.1017/jfm.2016.510 Published online by Cambridge University Press

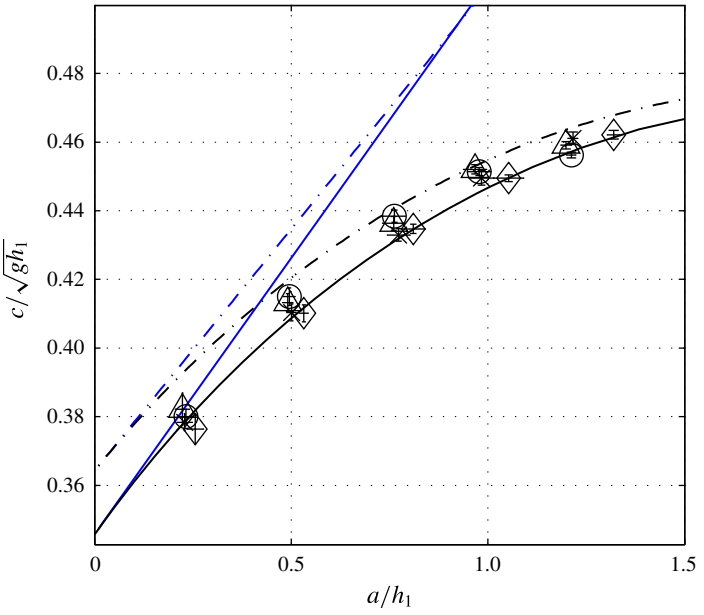


FIGURE 6. (Colour online) Measured wave speed c versus wave amplitude a of internal solitary waves, non-dimensionalized by $\sqrt{gh_1}$ and h_1 respectively: $\diamond$, data from the first and second wave probes; $\times$, data from the second and third wave probes; $\triangle$, data from the third and fourth wave probes; $\bigcirc$, data from the fourth and fifth wave probes. The error bars denoted by the short horizontal and vertical lines on top of symbols represent the standard deviations of five repeated measurements for the wave amplitude and the wave speed respectively. Black line, MCC-FS; black dashed line, MCC-RL; blue solid line, KdV-FS; blue dashed line, KdV-RL.

above the front half of the internal solitary wave, not right above or behind the trough of maximal displacement. The short surface waves form a wave packet with a representative wavelength of 3–4 cm, as shown in figure 5(*a*), The corresponding dimensionless wavelength and wavenumber are $\lambda_{obs}/h_1 = 0.6 \sim 0.8$ and $k_{obs}h_1 = 7.85 \sim 10.47$ respectively. No noticeable surface waves are detected on the free surface above the rear half of the solitary wave (figure 5*b*). The propagation of the short surface waves is recorded by a camcorder placed at $x/h_1 = 70$. It is difficult to measure the propagation speed of the surface wave packet precisely, but its speed is found to be approximately close to the wave speed of the internal solitary wave, as indicated by the straight line in figure 7. Therefore, one can imagine that the short surface waves are possibly generated by some action of the internal solitary wave.

To study the propagation of the short surface waves, we consider an internal solitary wave of $a/h_1 = 1.21$, for which the appearance of short surface waves is most evident. For an internal solitary wave of this wave amplitude travelling to the left, the wave speed is $c/(gh_1)^{1/2} \simeq 0.450$ from the MCC-FS model, while its linear long-wave speed is $c_0/(gh_1)^{1/2} \simeq 0.340$. It should be noticed that the solitary wave speed of the MCC-RL model is $c/(gh_1)^{1/2} \simeq 0.456$.

One possible scenario is a (linear) resonance mechanism between long internal waves and short surface waves, where the following condition is met:

$$c_0^- = c_g^+. \tag{5.1}$$

https://doi.org/10.1017/jfm.2016.510 Published online by Cambridge University Press

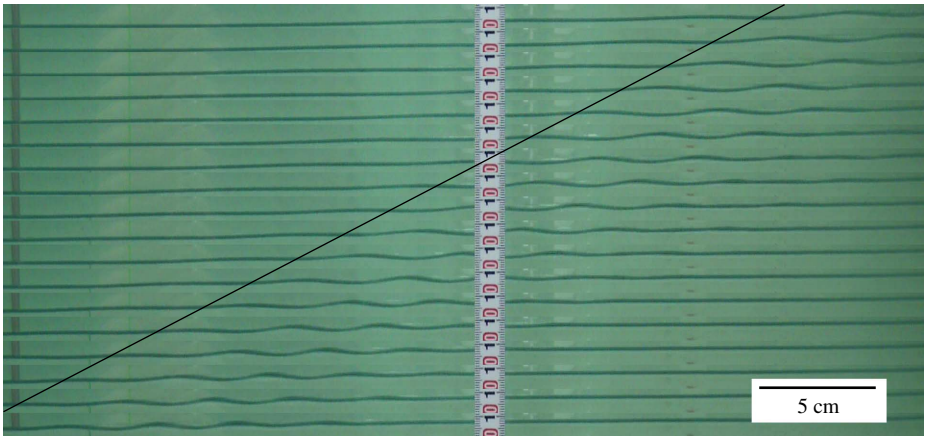


FIGURE 7. (Colour online) Combined snapshots of short surface waves recorded by a camcorder placed at $x/h_1 = 70$ for case 1.21. The snapshots were taken at every 4/60 s and the first snapshot is placed at the top of the picture. The straight line whose slope is the same as the internal solitary wave speed is added to show that the surface wave packet is propagating with the internal solitary wave.

Here, c_0^- is the linear long-internal-wave speed given by (2.16) and c_g^+ is the group velocity of (relatively) short surface waves, which can be found as described below. In a two-layer system with a top free surface, the wave frequency Ω for gravity–capillary waves can be found from

$$(\rho_1 + \rho_2 \coth kh_1 \coth kh_2)\Omega^4 - k\,[\rho_1 \hat{g}_1 \coth kh_1 + \rho_2 \hat{g}_1 \coth kh_2 + (\rho_2 - \rho_1)\hat{g}_2 \coth kh_1]\,\Omega^2 + (\rho_2 - \rho_1)\hat{g}_1 \hat{g}_2 k^2 = 0, \tag{5.2}$$

where k is the wavenumber and $\hat{g}_i$ are given by

$$\hat{g}_1 = g\left(1 + \frac{\gamma_1}{\rho_1 g}k^2\right), \quad \hat{g}_2 = g\left[1 + \frac{\gamma_2}{(\rho_2 - \rho_1)g}k^2\right], \tag{5.3a,b}$$

with γ_1 and γ_2 being the surface tension coefficients on the top free surface and the interface respectively. For the silicone oil used in the experiment, the surface tension coefficient at the top free surface is $\gamma_1 = 0.018$ N m^{-1} (compared with 0.0728 N m^{-1} for water) and the surface tension effect on short surface waves can be estimated as

$$\gamma_1 k^2/\rho_1 g \simeq 0.053, \tag{5.4}$$

where $k = 2\pi/4$ cm^{-1}, corresponding to the observed surface waves, has been used. Since this dimensionless parameter, or the inverse of the Weber number, is relatively small, the surface tension effect can be neglected. Then, the wave frequency for surface waves can be found from

$$(\rho_1 + \rho_2 \coth kh_1 \coth kh_2)\Omega^4 - \rho_2 gk(\coth kh_1 + \coth kh_2)\Omega^2 + (\rho_2 - \rho_1)g^2k^2 = 0, \tag{5.5}$$

whose solutions yield the following linear dispersion relations:

$$\Omega_\pm{}^2 = \frac{gk}{2(1 + \rho T_1 T_2)}\left[T_1 + T_2 \pm \sqrt{(T_1 + T_2)^2 - 4T_1T_2(1 - \rho)(1 + \rho T_1 T_2)}\right], \tag{5.6}$$

https://doi.org/10.1017/jfm.2016.510 Published online by Cambridge University Press

where $\rho = \rho_1/\rho_2 < 1$, $T_1 = \tanh(kh_1)$ and $T_2 = \tanh(kh_2)$. Here, the plus and minus signs correspond to the barotropic and baroclinic modes (or the surface-wave and internal-wave modes) respectively. With the group velocity of surface-mode waves $c_g{}^+ = \partial\Omega_+/\partial k$, the wavenumber k_{res} and the corresponding wavelength λ_{res} satisfying the linear resonance condition ($c_0^- = c_g^+$) in (5.1) can be found as $k_{res}h_1 \simeq 2.163$ and $\lambda_{res}/h_1 \simeq 2.904$ respectively. Alternatively, as it is relatively large, this resonant wavenumber can be estimated as $k_{res}h_1 \approx gh_1/(2c_0^-)^2$ from the dispersion relation for surface waves in deep water, for which the group velocity is given by $c_g^+ = (1/2)(g/k)^{1/2}$. Compared with the observed wavelength ($\lambda_{obs}/h_1 = 0.6 \sim 0.8$), the resonant wave is too long, and, therefore, the linear resonance mechanism is apparently unable to describe the appearance of short surface waves.

As the large-amplitude internal solitary wave induces a significant surface current u_s, the resonance condition accounting for the leading-order nonlinear effect might need to be modified to

$$c = c_g^+ + u_s. \tag{5.7}$$

It should be noticed that the linear long-wave speed c_0^- on the left-hand side of (5.1) is replaced by the speed of the solitary wave of MCC-FS, while the Doppler effect is included in estimating the group velocity of short surface waves. Under this modified resonance condition, the resonant wavenumber k_{res} is approximated by $k_{res}h_1 \approx gh_1/[2(c - u_s)]^2$. As the upper-layer horizontal velocity u_1 induced by the internal solitary wave varies in space, u_s is estimated as the upper-layer horizontal velocity at the location of the maximum displacement of the interface (at $X = 0$), so that $u_s/(gh_1)^{1/2} \simeq 0.261$. Even for the top free-surface case, as can be seen from (2.12)–(2.13), u_1 can be computed from (2.7), although the definition of η_1 should be modified to $\eta_1 = h_1 + \zeta_1 - \zeta_2$, where $\zeta_1/\zeta_2 \simeq -0.131$ from (2.17). Then, the resonant wavenumber and wavelength can be found as $k_{res}h_1 \simeq 6.998$ and $\lambda_{res}/h_1 \simeq 0.898$ respectively. In comparison with the observed wavelengths ($\lambda_{obs}/h_1 = 0.6 \sim 0.8$), the wavelength estimated by the modified resonant condition (5.7) gives a much better agreement. Nevertheless, it should be remarked that this result is based on a particular choice of u_s, which is the horizontal velocity of the upper layer at the maximal displacement ($X = 0$). For example, if the resonance condition is satisfied away from $X = 0$ where u_s is found to be smaller, a longer wave could be excited. Therefore, it remains to be explained how the surface waves possibly excited by the resonance mechanism evolve as they propagate with the internal solitary wave.

Here, as in Donato, Peregrine & Stocker (1999), ray theory is adopted to study the evolution of surface waves in a slowly varying current induced by an internal solitary wave. In the frame of reference moving with the internal solitary wave speed c, the background surface current is given, as the leading-order approximation, by $U(X) = u_1(X) - c$, so that

$$U(X) = -c\,\frac{h_1}{\eta_1}, \tag{5.8}$$

where $X = x - ct$. Then, the wave frequency of surface gravity waves in the moving frame is given by

$$\omega(k, X) = U(X)k \pm \Omega_+(k), \tag{5.9}$$

where the plus (or minus) sign corresponds to the right-going (or left-going) waves in the absence of surface current. Due to the presence of non-uniform current, the

https://doi.org/10.1017/jfm.2016.510 Published online by Cambridge University Press

wavenumber k no longer remains constant. Instead, from $\partial k/\partial t + \partial\omega/\partial X = 0$, the evolution of the local wavenumber k of surface gravity waves is governed by

$$\frac{\partial k}{\partial t} + (U \pm c_g^+)\frac{\partial k}{\partial X} + k\frac{\mathrm{d}U}{\mathrm{d}X} = 0. \tag{5.10}$$

Alternatively, along a ray path defined by

$$\frac{\mathrm{d}X}{\mathrm{d}t} = U(X) \pm c_g^+ = \frac{\partial\omega}{\partial k}, \tag{5.11}$$

equation (5.10) can be rewritten as

$$\frac{\mathrm{d}k}{\mathrm{d}t} = -kU'(X) = -\frac{\partial\omega}{\partial X}. \tag{5.12}$$

Then, as $\partial\omega/\partial t = 0$ from (5.9), the following holds for wave frequency ω:

$$\frac{\mathrm{d}\omega}{\mathrm{d}t} = \frac{\partial\omega}{\partial k}\frac{\mathrm{d}k}{\mathrm{d}t} + \frac{\partial\omega}{\partial X}\frac{\mathrm{d}X}{\mathrm{d}t} = 0, \tag{5.13}$$

where (5.11) and (5.12) have been used. This implies that ω remains unchanged along any ray. Thus, if it is initially uniform in space, the wave frequency must be uniform in space at a later time. In such a situation, the frequency is therefore constant in both space and time. Then, the variation of the local wavenumber k in X for given $U(X)$ can be seen along the level curves of ω, or the curves of constant ω, given by (5.9), from which one can understand how short surface waves are modulated by the non-uniform background current $U(X)$.

In figure 8, the level curves of ω given by (5.9) are shown for the right- and left-going surface waves. For the right-going waves (propagating in the direction opposite to that of the solitary wave in the fixed frame), they are shortened as they propagate through the current field induced by the solitary wave, but recover their original wavelengths as they propagate away from the internal solitary wave. On the other hand, for the left-going waves (propagating in the same direction as the internal solitary wave in the fixed frame), the change of the wavenumber is more substantial. The level curves originating from $x = -\infty$ in the moving frame show a sharp increase of the wavenumber as they approach the internal solitary wave, while the surface waves of small wavenumbers propagate much faster than the internal solitary wave so that they propagate to the left even in the moving reference frame with little interaction. It should be noticed that there are closed contours whose centres are located at $X/h_1 = 0$ and $kh_1 \simeq 6.998$, the critical points of (5.11) and (5.12). In fact, this is exactly the resonance condition at $X = 0$ given by (5.7). The existence of such closed contours implies that, once surface waves are excited possibly through the resonance mechanism and located above the internal solitary wave, the wavenumber increases rapidly in the front half of the internal solitary wave where $U'(X) < 0$. This shows the importance of the gradient of the surface current on the emergence of short surface wave packets.

As the wavenumber increases, the surface-wave amplitude is also expected to grow and, therefore, steep surface waves could be observed on the top surface located above the front half of the internal solitary wave, not right above or behind the wave trough, as mentioned previously. The location of a packet of short surface waves is consistent with our observation, but has not been clearly identified. Nevertheless, the

https://doi.org/10.1017/jfm.2016.510 Published online by Cambridge University Press

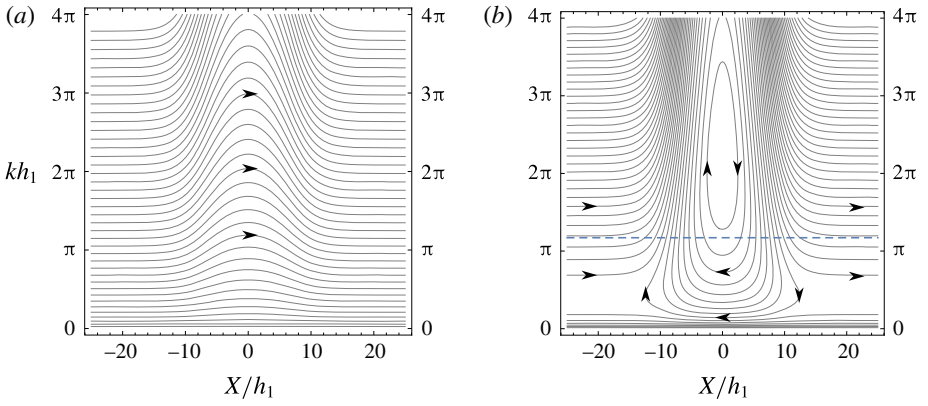


FIGURE 8. The level curves of ω given by (5.9) with the surface current induced by a solitary wave of $a/h_1 = 1.22$. (*a*) Right-going surface waves, (*b*) left-going surface waves.

appearance and the evolution of short surface waves still need to be investigated more systematically, but it should be remarked that the observed location of short surface waves is close to where the wavenumber increases rapidly. Moreover, if the surface waves become too steep, linear ray theory becomes invalid and the nonlinear effects have to be included for a complete explanation.

6. Conclusion

Internal solitary waves of large wave amplitudes have been studied experimentally in a system of two fluids, silicone oil and water, where the free-surface effects cannot be neglected due to a small but non-negligible density difference between the two fluids. The measured wave profiles and wave speeds using multiple wave probes are averaged over five repeated experiments to reduce measurement errors and are then validated with independent measurements using a digital camera. The measurements are also compared with both weakly nonlinear and strongly nonlinear long-internal-wave models with and without the rigid-lid assumption for the top surface. The weakly nonlinear KdV models show poor comparison for intermediate- and large-amplitude waves, while the strongly nonlinear MCC model with a rigid lid, often used for large-amplitude internal waves in a two-fluid system, predicts wider wave profiles. This discrepancy has been resolved by the MCC model with a free surface. As the density difference between the two fluids is non-negligible, it can be concluded that the top free surface has to be modelled correctly even for internal-wave motion.

When the wave amplitude is large, the rear half of the internal solitary wave suffers from the Kelvin–Helmholtz instability due to large shear across the interface, while the front half of the interface is smooth, as observed in previous experiments where the top surface is bounded by a rigid lid or the density difference between the two fluids is small. As the length scale of unstable internal waves on the interface is small, the baroclinic shear instability seems to be confined locally and little influenced by the presence of the top free surface. Nevertheless, the finite depth effect on baroclinic shear instability should be addressed with care (Barros & Choi 2014), and the stability characteristics of internal solitary waves under a free surface should be examined cautiously.

The propagation of fast barotropic surface waves is observed before the internal solitary wave is fully formed, but its reflection is greatly reduced by a wave absorber

https://doi.org/10.1017/jfm.2016.510 Published online by Cambridge University Press

at the end of the tank. Therefore, we should remark that the barotropic surface disturbances are reasonably well controlled, at least visually, in the experiment. Nevertheless, short surface wave packets have been observed as intermediate- or large-amplitude internal solitary waves are fully developed. This shows that the initial amplitude of surface disturbances is too small to be observed, but such disturbances could grow, by a certain mechanism, to form a localized packet propagating with the internal solitary wave. As the short surface waves are detected in cases 0.77 and 0.99, where no obvious KH instability is observed, it is assumed that the KH instability is not a direct cause of the appearance of such short surface waves. The resonance mechanism between long internal and short surface waves and the steepening mechanism due to slowly varying currents induced by internal solitary waves using ray theory are discussed to explain the appearance of the short surface wave packets on the top surface.

Nevertheless, the description of short surface wave packets should be improved and a more complete theory for the coupled surface- and internal-wave system should be developed, in particular including strong nonlinearity of the internal-wave motion. Unfortunately, no systematic measurements have been made here to find the relationship between the internal solitary wave amplitude and the characteristic amplitude and wavelength of short surface waves, including the critical amplitude of internal solitary waves beyond which short surface waves should be observed. In addition, no periodic surface waves are generated mechanically in our experiments. Considering an increased interest in surface signatures of internal solitary waves, an improved theoretical model along with systematic laboratory experiments on the interaction between periodic surface waves and internal solitary waves would be valuable.

Acknowledgements

The experimental work was supported by the National Research Foundation of Korea funded by the Ministry of Education, Science and Technology through the World Class University (WCU) program with grant no. R31-2008-000-10045-0. The authors would like to thank R. Barros for his help in computing the solitary wave solution of the MCC-FS model. T.K. was supported by a grant-in-aid for JSPS Fellows (23-3559) from the Japan Society for Promotion of Science (JSPS). T.W. was supported by Grants-in-Aid for Scientific Research of JSPS. W.C. gratefully acknowledges support from the Graduate School of Frontier Sciences for his visit to the University of Tokyo as a visiting scholar and the US National Science Foundation through grant no. DMS-1517456.

Appendix A. Derivation of the steady MCC-FS model

The horizontal momentum equations for the upper and lower layers given by (2.14)–(2.15) can be written in the following conserved forms:

$$v_{1t} + (u_1 v_1)_x + \left[g(\eta_1 + \eta_2) - \tfrac{1}{2}{u_1}^2 - \tfrac{1}{2}(D_1\eta_1 + D_1\eta_2)^2\right]_x = 0, \tag{A 1}$$

$$\left[v_2 + \rho\left(\tfrac{1}{2}\eta_1 D_1\eta_1 + \eta_1 D_1\eta_2\right)_x\right]_t + \left[u_2 v_2 + \rho\, u_1\left(\tfrac{1}{2}\eta_1 D_1\eta_1 + \eta_1 D_1\eta_2\right)_x\right]_x + \left[g(\rho\eta_1 + \eta_2) - \tfrac{1}{2}{u_2}^2 - \tfrac{1}{2}(D_2\eta_2)^2 - \rho\left(\tfrac{1}{2}(D_1\eta_1)^2 + (D_1\eta_1)(D_1\eta_2)\right)\right]_x = 0, \tag{A 2}$$

where $\rho = \rho_1/\rho_2$, and v_1 and v_2 are given by

$$v_1 = u_1 + \frac{1}{\eta_1}\left(\frac{1}{3}{\eta_1}^2 D_1\eta_1 + \frac{1}{2}{\eta_1}^2 D_1\eta_2\right)_x + \left(\frac{1}{2}D_1\eta_1 + D_1\eta_2\right)\eta_{2x}, \tag{A 3}$$

https://doi.org/10.1017/jfm.2016.510 Published online by Cambridge University Press

$$v_2 = u_2 + \frac{1}{\eta_2}\left(\frac{1}{3}{\eta_2}^2 D_2\eta_2\right)_x \tag{A 4}$$

respectively. It is interesting to notice that (A 1)–(A 2) can also be expressed in different forms. For example, (A 2) can be written as either

$$\begin{aligned}&\left(u_2 + \tfrac{1}{6}{\eta_2}^2 u_{2xx}\right)_t + \left[\tfrac{1}{2}{u_2}^2 + g(\rho\eta_1 + \eta_2)\right]_x \\ &\quad = \left[\tfrac{1}{2}{\eta_2}^2\left(u_{2xt} + \tfrac{2}{3}u_2 u_{2xx} - {u_{2x}}^2\right)\right]_x - \rho\left[\tfrac{1}{2}\eta_1({D_1}^2\eta_1) + \eta_1({D_1}^2\eta_2)\right]_x\end{aligned} \tag{A 5}$$

or

$$v_{2t} + (u_2 v_2)_x + \left[g(\rho\eta_1 + \eta_2) - \tfrac{1}{2}{u_2}^2 - \tfrac{1}{2}(D_2\eta_2)^2\right]_x + \rho\left[\tfrac{1}{2}\eta_1({D_1}^2\eta_1) + \eta_1({D_1}^2\eta_2)\right]_x = 0. \tag{A 6}$$

Equation (A 1) can be written similarly.

In addition, equations (2.14)–(2.15) yield physical conservation laws of linear momentum $\mathscr{P}$ and energy $\mathscr{E}$ (Barros & Gavrilyuk 2007):

$$(\rho_1\eta_1 u_1 + \rho_2\eta_2 u_2)_t + (\rho_1\eta_1{u_1}^2 + \rho_2\eta_2{u_2}^2 + \mathscr{P})_x = 0, \tag{A 7}$$

$$\left(\tfrac{1}{2}\rho_1\eta_1{u_1}^2 + \tfrac{1}{2}\rho_2\eta_2{u_2}^2 + \mathscr{E}\right)_t + \left[u_1\left(\tfrac{1}{2}\rho_1\eta_1{u_1}^2 + \mathscr{F}_1\right) + u_2\left(\tfrac{1}{2}\rho_2\eta_2{u_2}^2 + \mathscr{F}_2\right)\right]_x = 0, \tag{A 8}$$

where $\mathscr{P}$, $\mathscr{E}$ and $\mathscr{F}_i$ are given by

$$\begin{aligned}\mathscr{P} &= g\left(\tfrac{1}{2}\rho_1{\eta_1}^2 + \rho_1\eta_1\eta_2 + \tfrac{1}{2}\rho_2{\eta_2}^2\right) && \text{(A 9)}\\ &\quad + \rho_1\left(\tfrac{1}{3}{\eta_1}^2{D_1}^2\eta_1 + \tfrac{1}{2}\eta_1\eta_2{D_1}^2\eta_1 + \tfrac{1}{2}{\eta_1}^2{D_1}^2\eta_2 + \eta_1\eta_2{D_1}^2\eta_2\right) \\ &\quad + \tfrac{1}{3}\rho_2{\eta_2}^2{D_2}^2\eta_2, && \text{(A 10)}\\ \mathscr{E} &= \tfrac{1}{2}g(\rho_1{\eta_1}^2 + 2\rho_1\eta_1\eta_2 + \rho_2{\eta_2}^2) \\ &\quad + \tfrac{1}{2}\rho_1\eta_1\left[\tfrac{1}{3}(D_1\eta_1)^2 + (D_1\eta_1)(D_1\eta_2) + (D_1\eta_2)^2\right] + \tfrac{1}{6}\rho_2\eta_2(D_2\eta_2)^2, && \text{(A 11)}\\ \mathscr{F}_1 &= \rho_1\eta_1\left[g(\eta_1 + \eta_2) + \tfrac{1}{6}(D_1\eta_1)^2\right. \\ &\quad \left. + \tfrac{1}{2}(D_1\eta_1)(D_1\eta_2) + \tfrac{1}{2}(D_1\eta_2)^2 + \tfrac{1}{3}\eta_1({D_1}^2\eta_1) + \tfrac{1}{2}\eta_1({D_1}^2\eta_2)\right], && \text{(A 12)}\\ \mathscr{F}_2 &= \rho_2\eta_2\left[g(\rho\eta_1 + \eta_2) + \tfrac{1}{6}(D_2\eta_2)^2 + \tfrac{1}{3}\eta_2({D_2}^2\eta_2)\right. \\ &\quad \left. + \rho\eta_1({D_1}^2\eta_2) + \tfrac{1}{2}\rho\eta_1({D_1}^2\eta_1)\right]. && \text{(A 13)}\end{aligned}$$

For travelling waves, from (2.12)–(2.13) with (2.6), we have

$$u_{iX} = c\left(\frac{h_i}{\eta_i}\right)\left(\frac{\eta_{iX}}{\eta_i}\right), \quad u_{iXX} = c\left(\frac{h_i}{\eta_i}\right)\left(\frac{\eta_{iX}}{\eta_i}\right)_X - c\left(\frac{h_i}{\eta_i}\right)\left(\frac{\eta_{iX}}{\eta_i}\right)^2, \tag{A 14a,b}$$

$$G_i = -c^2\left(\frac{h_i}{\eta_i}\right)^2\left(\frac{\eta_{iX}}{\eta_i}\right)_X, \quad {D_i}^2\eta_j = c^2 h_i\left(\frac{h_i}{\eta_i}\right)\left(\frac{\eta_{jX}}{\eta_i}\right)_X. \tag{A 15a,b}$$

Then, by using these relationships, the four conservation laws given by (A 1), (A 2), (A 7) and (A 8) can be integrated in X once with imposition of zero boundary conditions at infinities, which yields the following four second-order differential equations:

$$\alpha_{j1}\eta_1'' + \alpha_{j2}\eta_2'' + \alpha_{j3}{\eta_1'}^2 + \alpha_{j4}{\eta_2'}^2 + \alpha_{j5}\eta_1'\eta_2' = \alpha_{j6} \quad \text{for } j = 1, 2, 3, 4, \tag{A 16}$$

where the prime denotes differentiation with respect to X. It should be noticed that equations (A 16) for $j = 1$, 2, 3 and 4 result from (A 1), (A 2), (A 7) and (A 8) respectively. In (A 16), the coefficients α_{jk} that depend on η_i are given by

https://doi.org/10.1017/jfm.2016.510 Published online by Cambridge University Press

$$\left.\begin{aligned}
&\alpha_{11}=\frac{1}{3}\frac{c^2{h_1}^2}{\eta_1},\quad \alpha_{12}=\frac{1}{2}\frac{c^2{h_1}^2}{\eta_1},\\
&\alpha_{13}=-\frac{1}{6}\frac{c^2{h_1}^2}{{\eta_1}^2},\quad \alpha_{14}=\frac{1}{2}\frac{c^2{h_1}^2}{{\eta_1}^2},\quad \alpha_{15}=0,\\
&\alpha_{16}=-g[(\eta_1-h_1)+(\eta_2-h_2)]+\frac{1}{2}c^2\left[1-\left(\frac{h_1}{\eta_1}\right)^2\right],
\end{aligned}\right\} \tag{A 17}$$

$$\left.\begin{aligned}
&\alpha_{21}=\frac{1}{2}\frac{\rho c^2{h_1}^2}{\eta_1},\quad \alpha_{22}=\frac{\rho c^2{h_1}^2}{\eta_1}+\frac{1}{3}\frac{c^2{h_2}^2}{\eta_2},\\
&\alpha_{23}=-\frac{1}{2}\frac{\rho c^2{h_1}^2}{{\eta_1}^2},\quad \alpha_{24}=-\frac{1}{6}\frac{c^2{h_2}^2}{{\eta_2}^2},\quad \alpha_{25}=-\frac{\rho c^2{h_1}^2}{{\eta_1}^2},\\
&\alpha_{26}=-g[\rho(\eta_1-h_1)+(\eta_2-h_2)]+\frac{1}{2}c^2\left[1-\left(\frac{h_2}{\eta_2}\right)^2\right],
\end{aligned}\right\} \tag{A 18}$$

$$\left.\begin{aligned}
&\alpha_{31}=\frac{1}{6}\rho c^2{h_1}^2\left(2+3\frac{\eta_2}{\eta_1}\right),\quad \alpha_{32}=\frac{1}{6}c^2{h_2}^2\left[2+3\rho\frac{{h_1}^2}{{h_2}^2}\left(1+2\frac{\eta_2}{\eta_1}\right)\right],\\
&\alpha_{33}=-\frac{1}{6}\frac{\rho c^2{h_1}^2}{\eta_1}\left(2+3\frac{\eta_2}{\eta_1}\right),\quad \alpha_{34}=-\frac{1}{3}\frac{c^2{h_2}^2}{\eta_2},\\
&\alpha_{35}=-\frac{1}{2}\frac{\rho c^2{h_1}^2}{\eta_1}\left(1+2\frac{\eta_2}{\eta_1}\right),\\
&\alpha_{36}=\rho c^2h_1\left(1-\frac{h_1}{\eta_1}\right)+c^2h_2\left(1-\frac{h_2}{\eta_2}\right)\\
&\qquad-\frac{1}{2}g\left[\rho{\eta_1}^2\left(1-\frac{{h_1}^2}{{\eta_1}^2}\right)+2\rho\eta_1\eta_2\left(1-\frac{h_1}{\eta_1}\frac{h_2}{\eta_2}\right)+{\eta_2}^2\left(1-\frac{{h_2}^2}{{\eta_2}^2}\right)\right],
\end{aligned}\right\} \tag{A 19}$$

$$\left.\begin{aligned}
&\alpha_{41}=\frac{1}{6}\rho c^3{h_1}^2\left[2\left(1-\frac{h_1}{\eta_1}\right)+3\frac{\eta_2}{\eta_1}\left(1-\frac{h_2}{\eta_2}\right)\right],\\
&\alpha_{42}=\frac{1}{2}\rho c^3{h_1}^2\left[1-\frac{h_1}{\eta_1}+2\frac{\eta_2}{\eta_1}\left(1-\frac{h_2}{\eta_2}\right)\right],\\
&\alpha_{43}=-\frac{1}{6}\frac{\rho c^3{h_1}^2}{\eta_1}\left(2+3\frac{\eta_2}{\eta_1}-\frac{h_1}{\eta_1}-3\frac{h_2}{\eta_1}\right),\\
&\alpha_{44}=-\frac{1}{6}\frac{c^3{h_2}^2}{\eta_2}\left(2-\frac{h_2}{\eta_2}+3\rho\frac{{h_1}^2}{{h_2}^2}\frac{h_1}{\eta_1}\frac{\eta_2}{\eta_1}\right),\\
&\alpha_{45}=-\frac{1}{6}\frac{c^3{h_2}^2}{\eta_1}\left[3\rho\frac{{h_1}^2}{{h_2}^2}+2\frac{\eta_2}{\eta_1}\left(1-\frac{h_2}{\eta_2}\right)\left(3\rho\frac{{h_1}^2}{{h_2}^2}-2\right)\right],\\
&\alpha_{46}=\frac{1}{2}\frac{\rho c^3h_1}{\eta_1}\left(1-\frac{h_1}{\eta_1}\right)^2+\frac{1}{2}\frac{c^3h_2}{\eta_2}\left(1-\frac{h_2}{\eta_2}\right)^2\\
&\qquad-\frac{1}{2}cg\left[\rho{\eta_1}^2\left(1-\frac{h_1}{\eta_1}\right)^2+2\rho\eta_1\eta_2\left(1-\frac{h_1}{\eta_1}\right)\left(1-\frac{h_2}{\eta_2}\right)+{\eta_2}^2\left(1-\frac{h_2}{\eta_2}\right)^2\right].
\end{aligned}\right\} \tag{A 20}$$

It should be noticed that (A 5)–(A 6) also give (A 16) with $j=2$.

https://doi.org/10.1017/jfm.2016.510 Published online by Cambridge University Press

In principle, from (A 16) with any two values of j, one can obtain a system of two nonlinear second-order differential equations for η_1 and η_2, but different combinations of j would result in different systems. This non-uniqueness is unacceptable; the systems must be identical. In fact, from (A 16) for $j = 1$ and 2, one can obtain the expressions for η_1'' and η_2'' as

$$\eta_i'' = q_i(\eta_1', \eta_2', \eta_1, \eta_2) \quad \text{for } i = 1, 2. \tag{A 21}$$

Then, by substituting these into (A 16) for $j = 3$ or 4, one can obtain the following first-order nonlinear differential equation in the form of

$$\beta_1 \eta_1'^2 + \beta_2 \eta_2'^2 + \beta_3 \eta_1' \eta_2' + \beta_4 = 0, \tag{A 22}$$

where the coefficients β_i are given by

$$\beta_1 = \rho c^2 h_1^2 \eta_2, \quad \beta_2 = c^2(h_2^2 \eta_1 + 3\rho h_1^2 \eta_2), \quad \beta_3 = 3\rho c^2 h_1^2 \eta_2, \tag{A 23a–c}$$

$$\begin{aligned} \beta_4 \;=\; & -3c^2[\eta_1(\eta_2 - h_2)^2 + \rho\eta_2(\eta_1 - h_1)^2] \\ & + 3g\eta_1\eta_2[(\eta_2 - h_2)^2 + \rho(\eta_1 - h_1)^2 + 2\rho(\eta_1 - h_1)(\eta_2 - h_2)]. \end{aligned} \tag{A 24}$$

It should be noticed that the left-hand side of (A 22) represents the Hamiltonian (Barros & Gavrilyuk 2007) for the system given by (A 21). The first three terms on the left-hand side of (A 22) represent the kinetic energy, while the last term β_4 is the potential energy.

REFERENCES

Barros, R. & Choi, W. 2014 Elementary stratified flow with stability at low Richardson number. *Phys. Fluids* **26**, 124107.

Barros, R. & Gavrilyuk, S. L. 2007 Dispersive nonlinear waves in two-layer flows with free surface. II. Large amplitude solitary waves embedded into the continuous spectrum. *Stud. Appl. Maths* **119**, 213–251.

Barros, R., Gavrilyuk, S. L. & Teshukov, V. M. 2007 Dispersive nonlinear waves in two-layer flows with free surface. I. Model derivation and general properties. *Stud. Appl. Maths* **119**, 191–211.

Benjamin, T. B. 1966 Internal waves of finite amplitude and permanent form. *J. Fluid Mech.* **25**, 97–116.

Camassa, R., Choi, W., Michallet, H., Rusas, P. & Sveen, J. K. 2006 On the realm of validity of strongly nonlinear asymptotic approximations for internal waves. *J. Fluid Mech.* **549**, 1–23.

Carr, M., Fructus, D., Grue, J., Jensen, A. & Davies, P. A. 2008 Convectively induced shear instability in large amplitude internal solitary waves. *Phys. Fluids* **20**, 12660.

Choi, W. & Camassa, R. 1996 Weakly nonlinear internal waves in a two-fluid system. *J. Fluid Mech.* **313**, 83–103.

Choi, W. & Camassa, R. 1999 Fully nonlinear internal waves in a two-fluid system. *J. Fluid Mech.* **396**, 1–36.

Donato, A. N., Peregrine, D. H. & Stocker, J. R. 1999 The focusing of surface waves by internal waves. *J. Fluid Mech.* **384**, 27–58.

Fructus, D., Carr, M., Grue, J., Jensen, A. & Davies, P. A. 2009 Shear-induced breaking of large internal solitary waves. *J. Fluid Mech.* **620**, 1–29.

https://doi.org/10.1017/jfm.2016.510 Published online by Cambridge University Press

GOULLET, A. & CHOI, W. 2008 Large amplitude internal solitary waves in a two-layer system of piecewise linear stratification. *Phys. Fluids* **20**, 096601.

GRUE, J., JENSEN, A., RUSS, P.-O. & SVEEN, J. K. 1999 Properties of large-amplitude internal waves. *J. Fluid Mech.* **380**, 257–278.

GRUE, J., JENSEN, A., RUSS, P.-O. & SVEEN, J. K. 2000 Breaking and broadening of internal solitary waves. *J. Fluid Mech.* **413**, 181–217.

KAO, T. W., PAN, F.-S. & RENOUARD, D. 1985 Internal solitons on the pycnocline: generation, propagation, and shoaling and breaking over a slope. *J. Fluid Mech.* **159**, 19–53.

KOOP, C. G. & BUTLER, G. 1981 An investigation of internal solitary waves in a two-fluid system. *J. Fluid Mech.* **112**, 225–251.

LIU, A. K., CHANG, Y. S., HSU, M.-K. & LIANG, N. K. 1998 Evolution of nonlinear internal waves in the East and South China Seas. *J. Geophys. Res.* **103**, 7995–8008.

LUZZATTO-FEGIZ, P. & HELFRICH, K. R. 2014 Laboratory experiments and simulations for solitary internal waves with trapped cores. *J. Fluid Mech.* **757**, 354–380.

MICHALLET, H. & BARTHELEMY, E. 1998 Experimental study of interfacial solitary waves. *J. Fluid Mech.* **366**, 159–177.

MIYATA, M. 1985 An internal solitary wave of large amplitude. *La mer* **23** (2), 43–48.

MIYATA, M. 1988 Long internal waves of large amplitude. In *Proceedings of the IUTAM Symposium on Nonlinear Water Waves* (ed. H. Horikawa & H. Maruo), pp. 399–406. Springer.

MONI, R. & KING, W. 1995 On the realm of validity of strongly nonlinear asymptotic approximations for internal waves. *Q. J. Mech. Appl. Maths* **48**, 21–38.

PETERS, A. S. & STOKER, J. J. 1960 Solitary waves in liquids having non-constant density. *Commun. Pure Appl. Maths* **13**, 115–164.

SEGUR, H. & HAMMACK, J. L. 1982 Soliton models of long internal waves. *J. Fluid Mech.* **118**, 285–304.

WALKER, L. R. 1973 Interfacial solitary waves in a two-fluid medium. *Phys. Fluids* **16** (11), 1796–1804.

https://doi.org/10.1017/jfm.2016.510 Published online by Cambridge University Press